ASTRONOMY
AND
ASTROPHYSICS

Fine phase resolved spectroscopy of the X-ray emission of the Crab pulsar (PSR B0531+21) observed with BeppoSAX

E. Massaro[1], **G. Cusumano**[2], **M. Litterio**[1], **and T. Mineo**[2]

[1] Istituto Astronomico, Universitá di Roma "La Sapienza", Unità FigCO-CNR, via G.M. Lancisi 29, 00161 Roma, Italy
[2] Istituto di Fisica Cosmica ed Applicazioni all'Informatica, CNR, via U. La Malfa 153, 90146 Palermo, Italy

Abstract. The Crab Nebula and the Pulsar have been pointed several times by the BeppoSAX satellite. We analysed all these observations, summed together, to study the main spectral properties with a good phase resolution. A new accurate estimate of the hydrogen column density in the Crab direction $N_H=3.23\times10^{21}\,\mathrm{cm}^{-2}$ is given as derived from the analysis of the off-pulse emission at low energies. We studied the changes of the spectral index with the pulse phase and showed that in the interpeak region it is systematically harder than in the main peaks of about 0.4. We observed also a significant spectral steepening of the pulsed emission and showed that this distribution can be represented by a unique law with a linear variable log slope and apply it to the spectrum of the first peak. A two component model is proposed to explain the phase evolution of the spectrum. One component has the same profile observed in the optical while the other presents a maximum at the phase 0.4 with essentially the spectrum of the interpeak region. Two possible interpretations for the origin of the latter component are discussed.

Key words: stars: pulsars: individual: PSR B0531+21 – X-rays: stars

1. Introduction

It is well known since early X-ray observations that the spectral energy distribution of the Crab pulsar (PSR B0531+21) is changing along with its double peak pulse profile. The intensity ratio of the second to the first peak increases from the soft X-rays up to the MeV region where it reaches the highest value (see the data archive of Massaro, Feroci & Matt 1997). The origin of this effect is not understood up to now. Pulse shapes have been computed for different accelerator sites: polar caps (Sturner & Dermer 1994, Daugherty & Harding 1996, Miyazaki & Takahara 1997), outer gaps (Chiang & Romani 1994, Romani & Yadigaroglu 1995) and closed magnetosphere (Eastlund et al. 1997). These theoretical profiles, in some cases symmetric, do not match the energy dependence of the peak intensity ratio and cannot explain the spectral changes across the pulse profile.

Send offprint requests to: T. Mineo (mineo@ifcai.pa.cnr.it)

A first phase resolved X-ray spectroscopy of the Crab pulsar was performed by Pravdo & Serlemitsos (1981) who used the data of one day long observation of OSO 8. More recent data, with a much finer phase resolution, were presented by Pravdo et al. (1997, hereafter PAH) who analysed the RossiXTE data between 5 and 250 keV.

The Italian-Dutch satellite BeppoSAX observed the Crab Nebula and Pulsar in 1996 during the Science Verification Phase (Mineo et al. 1997). From that epoch to the end of 1998 this source was pointed several times because it is used for a calibration check of the Narrow Field Instruments (hereafter NFI; for a detailed description of the scientific payload of BeppoSAX see Boella et al. 1997). All these observations, when summed together, provide a high statistics data set which can be used for a very accurate phase resolved spectroscopy of the pulsed emission over an energy range wider than two orders of magnitude, from about 0.1 up to 300 keV. In this paper we present the results of an accurate spectral analysis that shows in detail the relevant hardening of the spectral slope in the interpeak region with respect to the two main peaks. Our analysis is substantially more complete than PAH because of the wider energy band covered by BeppoSAX and the improved statistics due to a longer total exposure. We discuss, in particular, the spectral shape at energies lower than 4 keV and give a new accurate estimate of the absorbing column density in the Crab direction. Furthermore, we show that a single power law does not give an acceptable spectral fit over the entire range and that a better description can be achived using a countinously steepening spectral energy distribution. Finally, we also discuss that the change with phase of the spectral slope can be explained by the superposition of two emission components, likely originated in different regions of the magnetosphere.

2. Observations and data reduction

After the first observation of the Crab (1996 August - September), BeppoSAX pointed this source several times and collected a large amount of good quality data. The epochs of the pointings and the net exposure times for each NFI are given in Table 1. We recall, however, that after May 1997 the MECS operated with reduced sensitivity because of the failure of one of the three detector units. With respect to Mineo et al. (1997) the data set
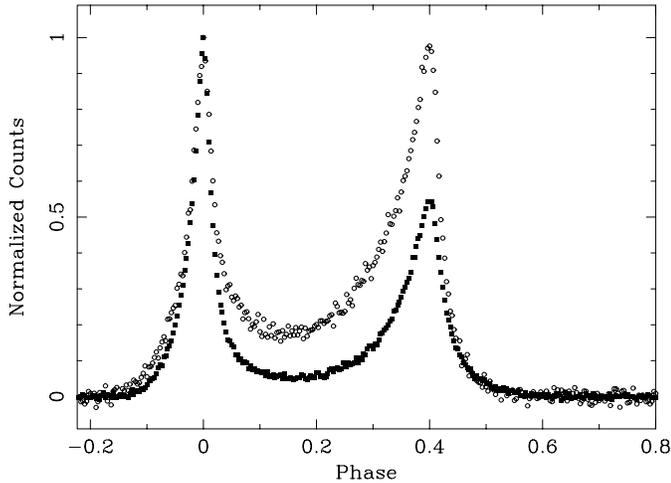
Fig. 1. Two summed X-ray pulse profiles of Crab in 300 phase channels in the energy ranges 1.5–5 keV (filled squares) and 100–300 keV (open circles). Both profiles are normalized to unity at the maximum of the first peak, after the subtraction of the off-pulse (0.6–0.83) constant level. Note the excess in the leading edge of first peak at higher energies.

Table 1. The BeppoSAX NFIs pointing epochs and the net exposure times of the Crab Pulsar.

Observation	Exposure Times (s)			
Date	LECS	MECS	HPGSPC	PDS
31 Aug 1996	–	–	28 384	27 749
6 Sep 1996	5 733	33 482	–	–
30 Sep 1996	–	7 874	–	6 305
11 Apr 1997	1 257	18 551	9 344	9 294
8 Oct 1997[a]	12 096	30 769	9 158	18 622
6 Apr 1998[a]	8 730	28 694	12 732	13 105
13 Oct 1998	–	–	–	14 916
Total exposure	27 816	119 370	59 618	89 991

[a] MECS operated with two detectors after May 1997.

has increased by factors ranging from 2.1 for the HPGSPC to about 4.9 for the LECS. Such great improvement of the statistics allows now to perform a fine resolved spectral analysis even in the interpeak region, where the pulsed signal is low, particularly at energies below a few keV.

For the imaging instruments we selected all the events within circular regions centered at the source position and having radii of 4′ (MECS) and 8′ (LECS). This choice corresponds to use a percentage of about 90% of the total source signal in both instruments, but it allows to apply the best tested spectral response matrices.

Phase histograms of the Crab pulsar were evaluated for each NFI and each pointing using the period folding technique. The UTC arrival times of all selected events were converted to the Solar System Barycentre with the DE200 ephemeris. The values of P and $\dot{P}$, for each observation epoch were derived from the Jodrell Bank Crab Pulsar Monthly Ephemeris (http://www.jb.man.ac.uk/). We constructed a large set of 300 bin phase histograms for every energy channel of each NFI.

The zero phase was fixed at the centre of the first peak, evaluated by means of gaussian fits. All the histograms for the same energy channel of each NFI were then added together. Before this operation we verified that all the profiles of the various observation epochs had fully compatible shapes and therefore similar folding accuracy. Two examples of summed pulse profiles for the MECS (1.5–5 keV) and PDS (100–300 keV), after the subtraction of a constant off–pulse signal, taken in the phase interval 0.6–0.83, and normalized to unity at the maximum of the first peak, are shown in Fig. 1. We stress, in particular, the improved S/N ratio of the data at energies greater than 100 keV, in comparison with those of PAH.

For the phase resolved spectral analysis we subtracted the mean off-pulse level from the content of each phase bin. Spectra were accumulated in phase intervals having a minimum width of 0.00667 (= 1/150). Whenever the count number is not high, in the interpeak region and in some energy ranges, wider phase intervals were taken in order to reduce the statistical uncertainty in estimating the spectral parameters. Furthermore, energy channels were rebinned up to have a minimum content of 20 counts.

The response matrices of all the NFIs used in our analysis are those relative to the November 1998 release. They are based on ground calibrations and MonteCarlo simulations and have been tested in flight with several well known X-ray sources (among which Cassiopeia A, 3C 273, NGC 4151, Vela X–1, Centaurus X–3, and the Crab Nebula itself). None of the NFI response matrices were adjusted in order to fit the Crab Nebula spectrum with a pre-defined power law, but this source was used as the other calibration sources to verify the goodness of the on-ground calibrations. (we thank F. Frontera, A. Parmar and A. Santangelo for information on this subject).

In the following we will shortly refer P1 and P2 for the first and second peak, respectively, and Ip for the bridge region between them. We stress that a standard definition for their phase widths is not existing, and we will conventionally adopt (-0.05,0.05) for P1 and (0.30,0.44) for P2. In any case, other phase intervals, when considered in our analysis, are always indicated in the text.

3. X-ray spectral properties

3.1. The off-pulse spectrum and the N_H estimate

An important quantity necessary for the spectral analysis at energies lower than a few keV is the intervening column density N_H. Although the Crab is one of the best studied X-ray sources this quantity is not well known. Several significantly different estimates based on various methods, ranging from 1.6×10^{21} cm^{-2} (Clark 1965) to 3.4×10^{21} cm^{-2} (Fritz et al. 1976), are reported in the literature. Recent estimates of the interstellar reddening agree for a mean $E(B - V)$ equal to 0.53 ± 0.04 (Blair et al. 1992, Gull et al. 1998). Assuming $R = A_V/E(B - V)$=3.09 (Rieke & Lebofsky 1985) and the N_H–to–A_V conversion by Predehl & Schmitt (1995), we obtain the value of 2.9×10^{21} cm^{-2}. If the conversion factor estimated by Gorenstein (1975), also reported by Zombeck (1990), is used, the column density increases up to 3.4×10^{21} cm^{-2}
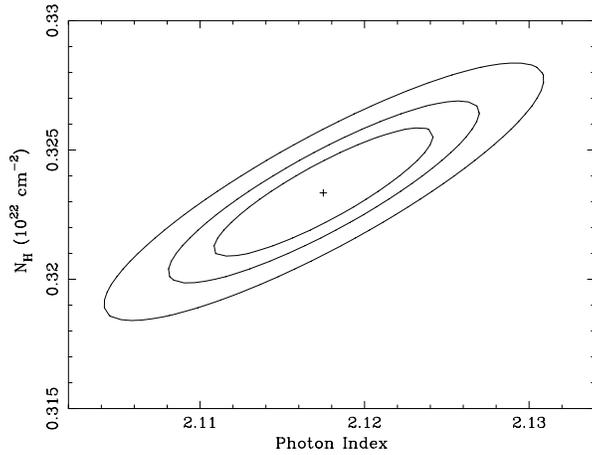
Fig. 2. Contour plot for the column density vs the power law spectral index derived from the LECS off-pulse spectrum (0.1–4 keV). The three contours correspond to 68, 90 and 99% confidence levels; the cross is relative to the best fit values of the two parameters.

We computed a new estimate of this quantity from Bep-poSAX data. To this aim we analysed the spectrum of the off-pulse region assumed representative of the nebular emission, which is well described by a single power law in a wide energy interval, practically covering all the entire BeppoSAX range, as it will be discussed in the following. A fit with an absorbed power law of the LECS data for energies between 0.1 and 4 keV gives a spectral index of 2.117 ± 0.004 and $N_H = (3.23 \pm 0.02) \times 10^{21}$ cm^{-2} with a reduced $\chi^2 = 1.3$ (364 d.o.f.). The contour plots for these two parameters are shown in Fig. 2; we can see that column densities smaller than 3.18×10^{21} cm^{-2} are evidently not compatible with a simple power law. If the value $N_H = 2.9 \times 10^{21}$ cm^{-2} is used the spectral index lowers to 2.04, but the reduced χ^2 reaches the largely unacceptable value of 2.5. Furthermore, the best fit spectral index of the MECS data between 4 and 7 keV is 2.117 ± 0.003 independently of the adopted N_H, coincident with that given above.

A value of N_H equal to 3.23×10^{21} cm^{-2} corresponds to a conversion factor with $E(B-V)$ of 6.09×10^{21} cm^{-2} mag^{-1}, about 20% greater than that of Predehl & Schmitt (1995), but closer to the one by Gorenstein (1975).

Finally we stress that N_H values of 3.0–3.2×10^{21} cm^{-2} were also found in the analysis of some ASCA observations of the Crab (Fukazawa et al. 1997). We are, therefore, confident that our result is likely the best available estimate of the actual column density and used it in the spectral analysis.

3.2. Phase evolution of the spectral indices

Phase dependent photon indices for single power laws were computed from the data of each instrument covering different energy ranges: LECS (0.1–4.0 keV), MECS (1.6–10 keV), HPGSPC (10–34 keV) and PDS (15–300 keV). The results are shown in the four panels of Fig. 3. The reduced χ^2 values are generally acceptable: they span the range between 0.8 and 1.25 with only four values over 127 fits greater than 1.25.
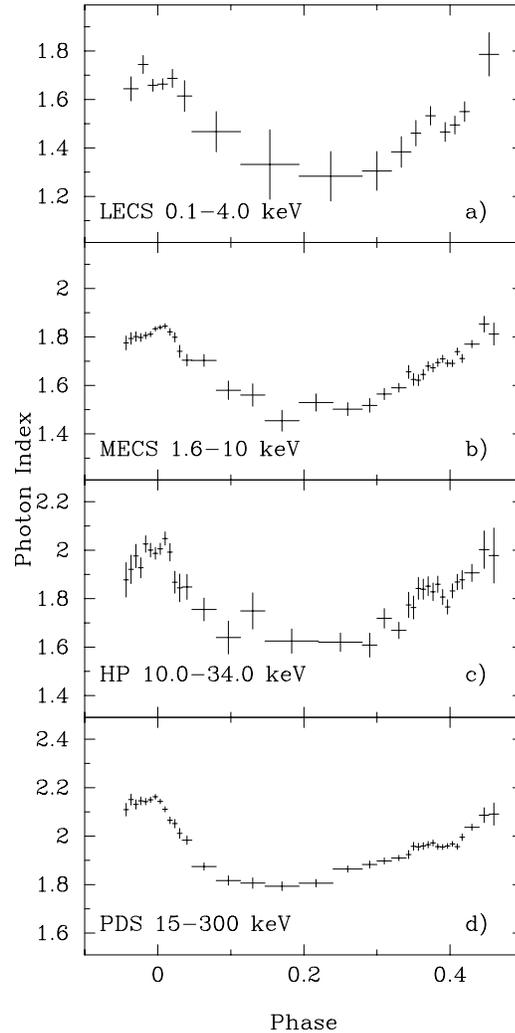
Fig. 3a–d. The phase resolved spectral index in the energy ranges of the four NFIs: LECS 0.1–4.0 keV panel **a**, MECS 2–10 keV panel **b**, HPGSPC 10.0–34.0 keV panel **c**, PDS 15–300 keV panel **d**.

We computed also the photon indices for two separate energy ranges of PDS, 16–80 keV and 80–300 keV, and the results are shown in Fig. 4. The same phase dependence is clearly apparent in each plot: the feature with the softest spectrum is P1, while the middle of the Ip is the hardest; the spectral index difference $\Delta\alpha$ is of the order of 0.30–0.45. Spectral indices are clearly increasing with energy over all the phase interval. In particular, that of P1 changes from 1.6 in the LECS range (Fig. 3a) to 2.3 at higher energies (Fig. 4b). The latest value is in good agreement with some other recent results above 100 keV like those of FIGARO II (Massaro et al. 1998) and CGRO (Ulmer et al. 1995). Note also that in Fig. 3c,d the central bins of P1 have a softer spectrum than the wings.

PAH reported similar results obtained with the PCA (5 - 60 keV) and HEXTE (16 - 250 keV) instruments on board RossiXTE. The phase evolution of the spectral index is nearly coincident with that found by us, but the spectrum steepening is not so clear as in our results. In particular, the P1 indices in
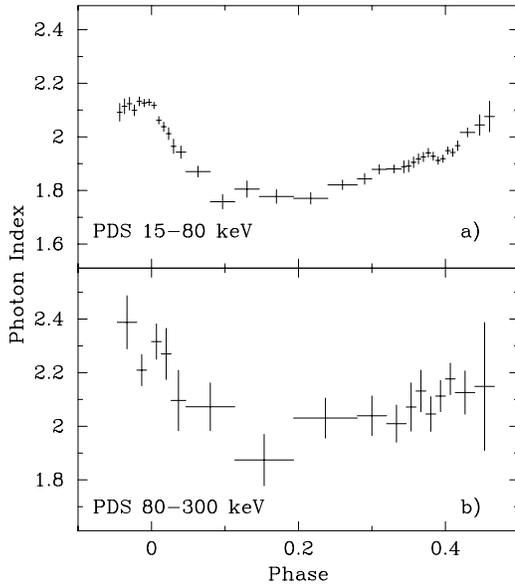
Fig. 4a and b. The phase resolved spectral indices in two PDS energy ranges: 16–80 keV (panel **a**) and 80–300 keV (panel **b**).

Fig. 5. Comparison of the photon indices of P1 (filled circles) with that of the nebula (open circles). The straight line corresponds to Eq. (2) when the best fit values of the parameters a and b are used.

the PCA and HEXTE data are 1.95 and 2.05. The latter value agrees with ours in the HPGSPC range (Fig. 3c) but it is smaller than that of the PDS (Fig. 3d, Fig. 4); the former is intermediate between those of MECS and HPGSPC, as expected by the different energy ranges and by the PCA lower threshold of 5 keV. The spectral indices of central Ip region are also in agreement with ours: the PCA value (1.62) coincides with to that of the HPGSPC, whereas the HEXTE value (1.75) is a bit smaller than ours, but the difference is not significant being within the HEXTE statistical uncertainty.

3.3. The spectrum of the first peak

It is already known that the spectral energy distribution of the total pulsed emission from Crab is continuously steepening from the optical frequencies to γ-rays with a maximum in the νF_ν plot in the MeV range (see, for instance, the review by Thompson et al. 1997). This distribution, however, is affected by the strong increase of P2 intensity with respect to P1.

As stated above, from the plots of Figs. 3 and 4 we see that the spectral indices in the various NFIs' energy ranges are significantly different, and therefore we expect that a single power law does not give a satisfactory representation of the spectral distribution over the entire BeppoSAX (0.1–300 keV) range. We studied, in particular, the spectrum of P1 which is the feature with the highest S/N ratio. We selected the events in a small phase interval 0.02667 wide, corresponding to eight bins over 300, centred at the maximum (zero phase). The reason for this choice, instead of the entire phase range of P1, is explained by the model described in Sect. 4. In this way we take only the bins where the P1 signal is stronger and minimize the possible contribution of a much harder component.

The best fit of a single power law obtained by taking the data of all the four instruments at the same time gives the not
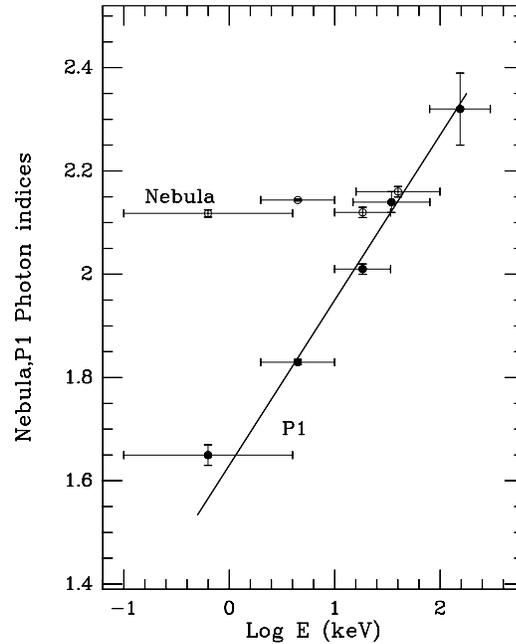
acceptable reduced χ^2 value of 3.5 (748 d.o.f.). Better fits are obtained when the NFIs are considered separately (Fig. 5). This great variation is not apparent for the corresponding indices of the off-pulse (or nebular) spectrum, whose values lie all in the narrow interval 2.12–2.16, with a typical statistical uncertainties of about 0.01 or less (Cusumano et al. 1998). The small but significant differences found among the fits of the various NFIs are likely due to systematic effect.

We tried then to represent the actual X-ray spectral distribution of P1 central bins with a continuously steepening law. The simplest model is likely the one having a linear dependence of the spectral slope upon the logarithm of the photon energy E:

$$F(E) = K(E/E_0)^{-(a+b\,Log\,(E/E_0))}, \qquad (1)$$

with only three free parameters because we fixed $E_0 = 1$ keV. We stress that the spectral indices shown in Fig. 3 indicate that a similar law should hold also at other phases; a more general model should so include the phase dependence of K, a, b. When Eq. (1) is fitted to the data of all NFIs selected as above in the phase interval (-0.0133, 0.0133), with the N_H value given in Sect. 3.1, a much better agreement is achieved. The reduced χ^2 lowers to 1.119 (747 d.o.f.) and the best fit values of the three parameters are: $a = 1.63 \pm 0.08$, $b = 0.16 \pm 0.04$ and $K = (8.87 \pm 0.07) \times 10^{-2}$ ph cm^{-2} s^{-1}. The fitted spectrum and the residuals are shown in Fig. 6. The χ^2 value, although acceptable, is two standard deviations greater than the expected one; this could be due to the occurrence of very small residual systematic effects that, with such a bright source can give a not negligible contribution to the χ^2.
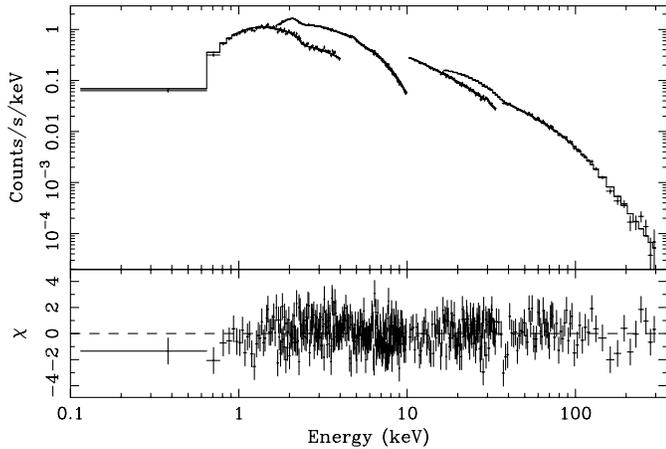
Fig. 6. The spectral fit of P1 using the law given in Eq. (1) over the wide energy range 0.1 - 300 keV covered by the four NFIs.

The energy dependent photon spectral index $\alpha(E)$ can be evaluated by the log derivative of Eq. (1):

$$\alpha(E) = a + 2\, b\, Log\,(E/E_0)\,, \tag{2}$$

that corresponds to the straight line plotted in Fig. 5.

We stress that the spectral distribution given by Eq. (1) with the best fit values of the parameters, is in principle valid only in the BeppoSAX range, where they were evaluated. Nevertheless, it reproduces the observed spectral shape when extrapolated to the UV-optical-IR range: the resulting energy spectral distribution is nearly flat at the photon energy of about 3 eV, corresponding to the photometric B band, and steepens toward the UV, in a good agreement with the results by Percival et al. (1993) and Gull et al. (1998). The extrapolated flux, however, is smaller than the observed one. The extrapolation of Eq. (2) at γ-ray energies (> 30 MeV) gives a photon index greater than 2.8, higher than the observed one equal to 2.05±0.03 (Fierro 1995). This value is also smaller than that found by us for the PDS data and implies that the P1 spectrum flattens in the MeV region.

4. A two component model

In order to explain the behaviour of the spectral index with the phase, PAH proposed a scenario where the X-ray emission is originated by particles accelerated in the polar cap region just above the neutron star surface. The geometry of the emission beam is a hollow cone with the axis coaligned to the magnetic one and the two main peaks correspond to the crossing of the cone annulus by the line of sight. According to these authors the resulting spectrum is harder in the Ip where the emission is pure curvature radiation not softened by the contribution from the e^+ e^- cascade, more relevant close to the outer rim. This interpretation, however, faces with some difficulties: the similar spectral behaviour of P2 and Ip and the spectral hardening of the P1 leading edge with respect to the central bins.

We followed a different approach and considered that the observed pulsed emission is due to the superposition of two com-

ponents having different phase distributions and energy spectra. The first component is assumed to have the same pulsed profile observed at optical frequencies (Smith et al. 1988, Percival et al. 1993), with P1 much more prominent than P2 and a very low intensity in the Ip region. A similar shape is also observed at energies greater than 30 MeV even if the profile of P2 is slightly different (Fierro et al. 1998) suggesting that the electron populations emitting in both energy ranges. We will refer to this component in the following as the optical one (shortly C_O). The second component (hereafter C_X) is assumed to have the greatest relative intensity in the hard X - low energy γ rays and it is, therefore, responsible of the P2/P1 change. We derived its phase profile in order to reproduce the observed one when summed to C_O: we found that C_X increases monotonically up to the phase 0.4 and then has a sharp cut-off. The main properties of the latter component were then estimated from the BeppoSAX data, essentially by means of a fitting procedure of several pulse profiles at different energies, as described in detail in the following subsections.

4.1. The components' shapes

The study of C_X is easier if an analytical representation for it is used. At the beginning we assumed that its phase distribution is substantially independent of energy and therefore it is possible to write the C_X intensity as the product of two functions one dependent only on the photon energy E and the other on the phase f:

$$I_X(E, f) = Y(E)\, g(f)\,, \tag{3}$$

The whole phase interval where C_X is not zero is denoted by (f_1, f_4) and is divided by two inner points at the phases f_2 and f_3 into three segments: in (f_1, f_2) the C_X shape is given by a power law, in (f_2, f_3) by an exponential function, joining the first one at f_2 and finally a linear descending branch from f_3 to f_4 connects the maximum to the zero level of the off pulse. We have

$$g(f) = \exp\{p(f_2 - f_3)\} \left(\frac{f - f_1}{f_2 - f_1}\right)^s\,, \tag{4a}$$

for $f_1 < f < f_2$, and

$$g(f) = \exp\{p(f - f_3)\}\,, \tag{4b}$$

for $f_2 < f < f_3$.

We verified also if all the parameters of $g(f)$ are really independent of the photon energy. This assumption resulted quite correct for the phase interval boundaries, taken equal to $f_1 = -0.15$, $f_2 = 0.21$, $f_3 = 0.40$, $f_4 = 0.43$ and the power law exponent $s = 0.4$. Note that with this choice C_X is non zero also in the phase interval of P1: it is necessary to explain the broadening of this peak with increasing energy and the softer spectrum of the peak centre with respect to both wings. As it will be described in Sect. 4.2, we found that a better agreement with the data is obtained if also p is allowed to vary: it changes from about 11. in the keV range to 8. above 150 keV. The factorisation of Eq. (3), even if largely acceptable, does not give
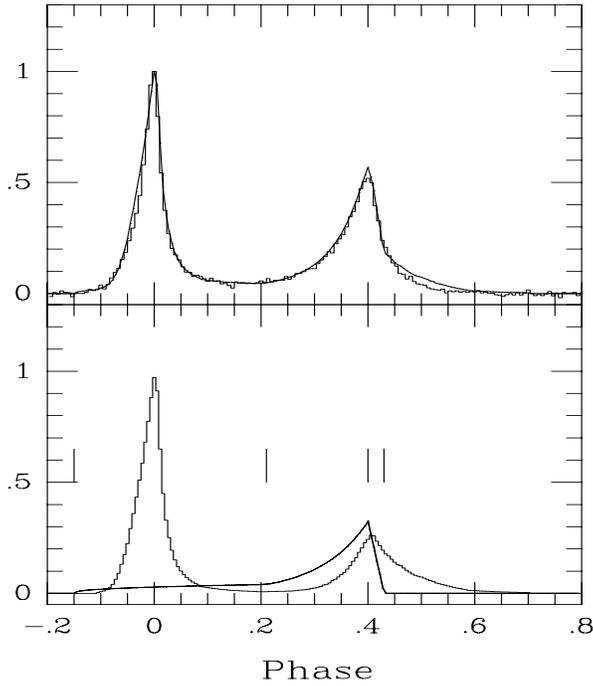
Fig. 7. Comparison between the observed pulse profile in the energy interval (1.0–1.95) keV and the two component model profile, computed for the mean energy of 1.6 keV (upper panel). The phase distributions of C_O and C_X with the proper normalisation are shown in the lower panel; the four vertical bars indicate the phases from f_1 to f_4.

a very precise description of the pulse profiles, suggesting that the shape of C_X cannot be considered completely independent of the energy.

The estimates of Y and p were obtained by means of quadratic minimization of the differences with the measured profiles in the (f_2, f_3) interval only. The algorithm was slightly more complicated than usual because we worked with profiles normalized to the P1 maximum and then C_X contributes to the normalization itself. For a given values of E and p, Y was estimated by the formula

$$Y = \frac{\sum_i [(I_O(f_i) - I(f_i)(AI_O(f_i) - e^{\{p(f_i - f_3)\}})]}{\sum_i [(AI(f_i) - e^{\{p(f_i - f_3)\}})(AI_O(f_i) - e^{\{p(f_i - f_3)\}})]} \quad (5)$$

where the sum is over all the considered phase bins, I and I_O indicate the observed X-ray and C_O profiles, respectively, and

$$A = g(0) = 0.705 \exp\{-0.19\,p\}. \quad (6)$$

We also tried a model with a power law instead of the exponential function of Eq. (4b) but, because no improvement was found with respect to the above formula, it will not be considered in further analyses.

4.2. The total profile

Three examples of pulse profiles computed using the two component model are shown in the upper panels of Figs. 7, 8 and 9 together with 150 bin histograms of the BeppoSAX data for the three energy intervals (1.0–1.95), (8.0–10.0), (57.–102.) keV.
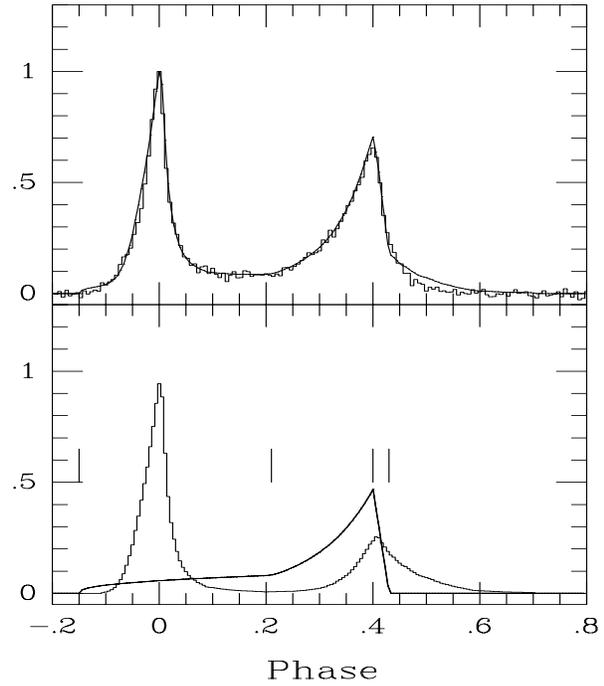
Fig. 8. The same as Fig. 7 but for the energy interval (8.0–10.0) keV and a model pulse profile computed for the mean energy of 8.85 keV.
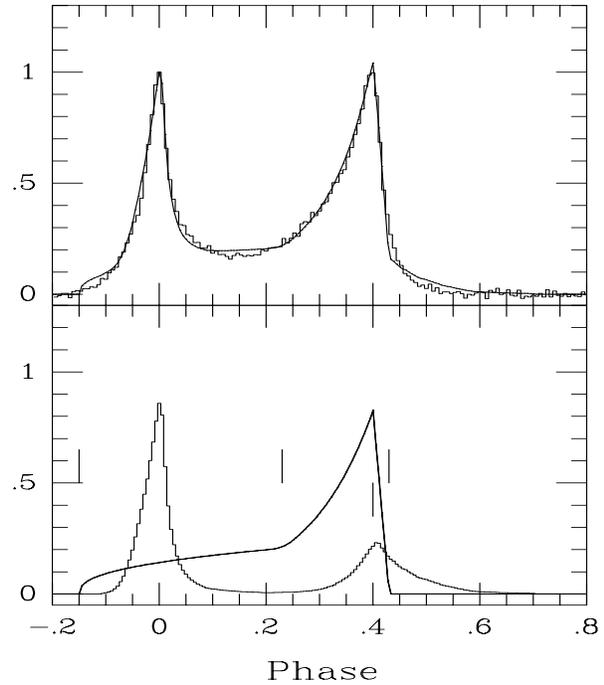
Fig. 9. The same as Fig. 7 but for the energy interval (57.–102.) keV and a model pulse profile computed for the mean energy of 75.2 keV.

The lower panel of each figure shows C_O and C_X separately: their relative intensities have been scaled in order to obtain a total value at the zero phase equal to unity. The values of p and Y used in the computations are those corresponding to the mean energies weighted with the detected counts. The agreement with the data is satisfactory in the whole energy range covered by

Fig. 11. The photon index vs phase in the MECS band expected from the two component model (solid line) compared with the results of Fig. 3b.

Fig. 10. The energy dependence of the parameters Y (upper panel) and p (lower panel); the power law best fit of the former is also shown.

BeppoSAX even if some small discrepancies are apparent. For example, the leading edge of P1 and the trailing edge of P2 do not match well the data. These discrepancies, likely due either to the analytical model of C_X or to the optical profile itself, are practically unavoidable unless one adopts a very *ad hoc* model.

In the upper panel of Fig. 10 we plotted Log Y vs Log E: a single power law gives a good representation of the trend and the resulting exponent is 0.28. In Fig. 10 (lower panel) the values of the coefficient p are also shown. Its monotonically decrease indicates that the leading edge of P2 becomes shallower and shallower with increasing energy.

A more careful analysis showed also that the Ip intensity is even better represented if f_2 is slightly changed with energy from the above value: the range remains narrow, from 0.20 at the lowest energies to 0.23 at the highest one, without significant differences of the Y and p values. These improvements, however, are quite small and therefore only the shape parameter p has to be considered significantly dependent upon energy.

4.3. The spectral index

The different spectral and phase distributions of the two components would consistently reproduce the phase dependence of the spectral index described in Sect. 3.2. This can be easily seen in Fig. 11 where our data in the MECS band are compared with the model expectations. The model photon index was simply computed from the ratio of the summed intensities of C_O and C_X at the two extreme energy values:

$$\alpha_{12} = \frac{Log(I(E_2)/I(E_1))}{Log(E_2/E_1)} + \alpha_O. \tag{7}$$

Since we used normalised pulse profiles our slope is identically equal to zero at the centre of P1 and we added, therefore, the constant α_O=1.83 to our results in order to match the measured values. The agreement between the observed points and the model is fully satisfactory, in particular for the softness of the P1 core with respect to the wings. The presence of a hard pedestal in the same phase interval of P1 is likely the simplest explanation of this asymmetry between the two peaks that cannot simply explained by the hollow cone model of PAH. Our results show that to reproduce the observations, the spectrum of this pedestal must be similar to that of Ip and P2 and therefore it is reasonable to consider them all as belonging to the same component.

5. Discussion

The BeppoSAX observations of the Crab pulsar have provided one of the best data set for a detailed study of the spectral and phase distributions over a wide X-ray energy interval. Using these data we derived the phase evolution of the spectral slope in several energy ranges. In particular, we confirmed that the spectral index is not constant within the phase interval of P1 and that both the leading and trailing edges have harder spectra than the central bins. Furthermore, we showed that the P1 spectral index changes from 1.65 to 2.3, for energies of about 0.5 keV to more than 200 keV. A law with a linearly varying spectral index gives a satisfactory representation of this behaviour.

The interpretation of all these findings in terms of a consistent physical model is not simple. A first step in this direction is the understanding if such complex behaviour is due to fact that we are observing photons emitted in different regions of the magnetosphere and likely by different emission mechanisms.

To this aim we showed that, at least as a first approximation, the shape of X-ray pulse profiles of the Crab with the energy can be explained by the superposition of two components with different phase and energy distributions. The major success of this model is that it gives a very simple explanation for the spectral index evolution with the phase. In particular, the soft core of P1 follows directly by the presence of the harder C_X pedestal.

From the energy dependence of the relative component intensities we can conclude that the X-ray spectrum of C_X can be approximately described by a law similar to that of P1, but with a spectral index systematically flatter by 0.28, so in the 2–10 keV range it would be equal to 1.55 and to about 2.0 around 200 keV. The C_X spectrum should have a cut-off above this energy, likely above a few MeV, as indicated by COMPTEL data (Much et al. 1995). It is also possible that C_X should be also detectable at lower energies, down to optical frequencies, as suggested by the small residual flux in the Ip region.

Open problems are the nature of the emission mechanisms and the locations in the magnetosphere for both these components. In the following we will limit our discussion only to C_X, independently of the C_O origin. We propose two possible hypotheses; one based on the spectral distribution and the other on the phase profile. A more complete model of the Crab emission is beyond the aim of the present paper.

Zhu & Ruderman (1997) have shown that a copious production e^+e^- pairs can occur in the closed magnetosphere not far from the neutron star surface. Curvature photons, emitted by high energy particles leaving the acceleration site and moving toward the star along the field lines, make pairs where the transverse magnetic field becomes large enough to absorb them and perhaps colliding with X-ray photons from the star. These pairs emit immediately synchrotron photons in the X-ray band and the expected photon index is close to 1.5 if the emitting particles are only those of the first generation (Wang et al. 1998). Furthemore, these authors argue that the upper spectral cut-off should be in the MeV range. This spectral behaviour is quite similar to the one we derived for C_X and it is suggestive for such possible origin. Wang et al. (1998) noticed also that hard X-ray components with similar photon indices are present in two other γ-ray pulsars (Geminga, PSR 1055-52) and associated it with this class of pulsars because of the e^+e^- pairs production on closed field lines in the neighbouring of the neutron star. It is then natural that such a component could also be present in the Crab. More recently, Cheng & Zhang (1999) have shown that if more pair generation are considered the photon index can change from 1.5 to 1.9. The computation of the phase distribution, however, is a difficult task because the geometry of the emission region and the radiation pattern can be quite complex.

Our other hypothesis on the C_X origin is based upon its shape and particularly the sharp cut-off beyond the phase 0.4. The observed phase distribution is affected by the relativistic aberration which becomes stronger and stronger approaching the light cylinder (Cheng et al. 1986) and gives a phase shift of about 0.25. It is not difficult to show that the phase distribution of photons emitted radially in a region close to the light cylinder is similar to that of C_X. An example of this ef-
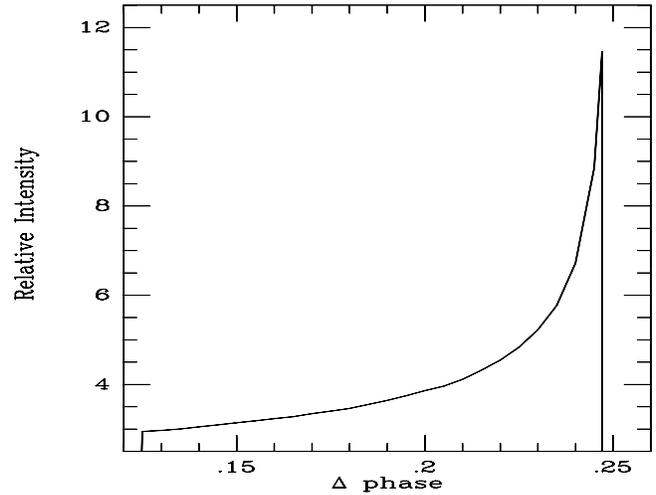
Fig. 12. The expected phase distribution of photons due to the aberration shift and travel time effects. Photons are emitted radially in a plane perpendicular to the rotation axis from a region between 0.4 and 0.99 of the light cylinder.

fect is plotted in Fig. 12, and the mathematical justification is given in the Appendix. Computations were carried out for a simple geometry approximating what was expected from particles streaming along the outer gap field lines. We assumed that photons are emitted in a plane perpendicular to the rotation axis, in the radial direction with a δ-like angular distribution in a region between 0.4 and 0.99 of the light cylinder. The resulting profile covers a phase interval narrower than that we derived for C_X, about equal to 0.5. This discrepancy can be solved by assuming an extended emitting region and a not radial radiation pattern to achieve a combined phase width of about 0.3–0.4. This scenario is in conflict with the previous one because the emitting particles cannot be locally produced pairs this process being inhibited by the relatively low magnetic field.

In conclusion we stress that the Crab pulsar would offer the interesting possibility to observe at the same time radiation emitted by different mechanisms in various regions of the magnetosphere. Fine resolved spectroscopy is likely the best way to study in detail these processes. It is important to extend it to higher energies, hopefully to the MeV range where the spectra of the components change, to achieve more information for determining the component parameters and understanding the emission processes. The next scheduled INTEGRAL mission is one of the best opportunities to obtain very important data in this range.

Appendix A: aberration effect in the phase distribution

The observed phase of a photon is given by the sum of three terms (Cheng et al. 1986): the emission phase $\overline{\varphi}$, an aberration

term φ_a and a flight path difference term φ_t. Suppose that at a point $\vec{x}(\bar{r}, \bar{\theta}, \overline{\varphi})$ rotating with velocity $v = \beta c = \Omega \bar{r} \sin \bar{\theta}$ (Ω being the spinning velocity of the pulsar) a photon is emitted with 4-momentum $k^\mu = \omega(1, \sin \theta \cos \varphi, \sin \theta \sin \varphi, \cos \theta)$ in the corotating frame. Then, assuming that photons are emitted along the radial direction ($\theta = \bar{\theta}$, $\varphi = \overline{\varphi}$) and neglecting any field bending, one gets the following simplified expressions:

$$\Delta\varphi_a = \arctan(\gamma\Omega\bar{r}/c) = \arctan(\beta\,\gamma\,\csc\theta) \tag{A.1}$$

$$\Delta\varphi_t = (\Omega\bar{r})/(\gamma c) = \frac{\beta\,\csc\theta}{\gamma} \tag{A.2}$$

where γ is the Lorentz factor of the local rotating frame. Thus the total observed phase (in units of 2π and taking $\varphi=0$) of the photon results to be:

$$f = \frac{1}{2\pi}(\Delta\varphi_a + \Delta\varphi_t) \tag{A.3}$$

The resulting range of f is then from 0 to 0.25. Suppose that photons are emitted in the interval $0 < r_1 \le \bar{r} \le r_2 < c/\Omega \sin\bar{\theta}$ with some distribution function $dN(\bar{r}) = \psi(\bar{r})d\bar{r}$. By using $v = \Omega\bar{r}\sin\bar{\theta}$ and neglecting the $\bar{\theta}$ – dependence of r along the field – line, this will become $dN(f) = n(f)df$, with:

$$n(f) = \psi(\bar{r})\frac{d\bar{r}}{df} \,. \tag{A.4}$$

Thus, even if $\psi(\bar{r})$ is constant (assumed unity) the distribution of the photons with the phase will be non–trivial.

After calculating the derivative of Eq. (A.3), the following expression for $n(\beta) = 1/\partial_\beta f$ is found:

$$n(\bar{r}) = \frac{2\,\pi c}{\gamma\Omega sin\theta}\frac{1 + \beta^2 \cot^2 \theta}{1 + (1 - 2\beta^2)(1 + \beta^2 \cot^2 \theta)} \,. \tag{A.5}$$

The final result for Eq. (A.4) is obtained by combining (A.5) with (A.3) and can be computed numerically.

References

Boella G., Butler R.C., Perola G.C., et al., 1997, A&AS 122, 299
Blair W.P., Long K.S., Vancura O., et al., 1992, ApJ 399, 611
Cheng K.S., Ho C., Ruderman M., 1986, ApJ 300, 500
Cheng K.S., Zhang L., 1999, ApJ 515, 337
Chiang J., Romani R.W., 1994, ApJ 436, 754
Clark B.G., 1965, ApJ 142, 1398
Cusumano G., Mineo T., Segreto A., et al., 1998, in: Scarsi L., et al. (eds.), The Active X-ray Sky, Nucl. phys. B (Proc. Suppl.) 69, 265
Daugherty J.K., Harding A.K., 1996, ApJ 458, 278
Eastlund B.J., Miller B., Curtis Michel F., 1997, ApJ 483, 857
Fierro J.M., 1995, PhD Thesis, Stanford Univ.
Fierro J.M., Michelson P.F., Nolan P.L., et al., 1998, ApJ 494, 734
Fritz G., Meekins J.F., Chubb T.A., et al., 1976, ApJ 164, L55
Fukazawa Y., Ishida M., Ebisawa K., 1997, ASCA News 5, 1
Gorenstein P. 1975, ApJ 198, 95
Gull T.R., Lindler D.J., Crenshaw D.M., et al., 1998, ApJ 495, L51
Massaro E., Feroci M., Matt G., 1997, A&AS 124, 123
Massaro E., Feroci M., Costa E., et al., 1998, A&A 338, 184
Mineo T., Cusumano G, Segreto A., et al., 1997, A&A 327, L21
Miyazaki J., Takahara F., 1997, MNRAS 290, 49
Much R., Bennett K., Buccheri R., et al., 1995, A&A 299, 435
Percival J.W., Biggs J.D., Dolan J.F., et al., 1993, ApJ 407, 276
Pravdo S.H., Angelini L., Harding A.K. (PAH), 1997, ApJ 491, 808
Pravdo S.H., Serlemitsos P.J., 1981, ApJ 246, 484
Predehl P., Schmitt J.H.M., 1995, A&A 293, 889
Rieke G.H., Lebofsky M.J., 1985, ApJ 288, 618
Romani R.W., Yadigaroglu I.-A., 1995, ApJ 438, 314
Smith F.G., Jones D.H.P., Disck J.S.B., at al., 1988, MNRAS 233, 305
Sturner S.J., Dermer C.D., 1994, ApJ 420, L79
Thompson D.J., Harding A.K., Hermsen W., et al., 1997, in: Dermer C.D., Strickman M.S., Kurfess J.D. (eds.), Proc. 4th Compton Symp., AIP Conf. Proc. 410, 39
Ulmer M.P., Matz S.M., Grabelsky D.A., et al., 1995, ApJ 448, 356
Wang F.Y.-H., Ruderman M., Halpern J.P., et al., 1998 ApJ 498, 373
Zombeck M., 1990, Handbook of space astronomy and astrophysics, Cambridge: Univ. Press
Zhu T., Ruderman M., 1997, ApJ 478, 701